Bimetallic organic framework-derived rich pyridinic N-doped carbon nanotubes as oxygen catalysts for rechargable Zn-air batteries

Changgan Lai[1], Xianbin Liu[1], Ying Wang[1], Changqing Cao[1], Yanhong Yin[1], Xinhua Liu[2,3], Billy Wu[2], Shichun Yang[3] and Tongxiang Liang[1]

[1]*School of Materials Science and Engineering, Jiangxi University of Science and Technology, 86 Hongqi Road, Ganzhou 341000, P. R. China*

[2]*Dyson School of Design Engineering, Imperial College London, South Kensington, SW7 2AZ, London, UK*

[3]*School of Transportation Science and Engineering, Beihang University, Beijing, China*

Abstract

Oxygen-evolution and oxygen-reduction reactions (ORR and OER) represent the two important cornerstones of many renewable energy technologies. As the traditionally used noble metal based electrocatalysts are becoming unsustainable, it is a challenge not only to limit the use of precious metals but to perform both ORR and OER using the same catalysts without compromising catalytic activity, stability and cost-efficiency. Clearly, future commercial viability of these technologies heavily depends on the development of bifunctional electrocatalysts that address the above limitations. Here, a route to ultrafine bimetallic Ni_xCo_3 nanocrystals embedded in pyridinic nitrogen enriched carbon nanotubes, namely Ni_xCo_3@N-CN, via metal organic framework is reported. The Ni in the bimetallic nanocrystals is found to favor the doping of pyridinic nitrogen in high amounts (~5.62 %), which is a key enabler for high catalytic activity. When tested as electrocatalysts for OER, Ni_xCo_3@N-CN composites offered a lower OER onset potential ~1.52 V at a current density 10 mA/cm^2 and faster kinetics (a lower Tafel slope of 56 mV/decade). When tested for ORR activity, the superior oxygen electrocatalytic performance of Ni_xCo_3@N-CN was shown by achieving a more favorable half-wave potential of 0.85 V and a large diffusion limiting current density of 4.73 mA/cm^2 and high catalytic stability (20,000s with high current retention). This is attributed to the hierarchically built structure that allows for the dispersion of ultrafine Ni_1Co_3 bimetallic nanocrystals, high pyridinic nitrogen doping, highly networked electron pathways, high surface area

(active sites) and their synergistic function. These findings point to a promising research avenue for developing low-cost and high-performance bifunctional oxygen electrocatalyst for renewable energy.

Keyword: Bifunctional oxygen electrocatalyst, pyridinic N doping, bimetallic nanoparticles, metal carbon nanotube composite, metal organic framework

Introduction

With ever growing energy consumption and environmental pollution, developing next-generation renewable energy storage and conversion technologies is an urgent task. On account of their high efficiency and zero-emission characteristics, fuel cells and metal-air batteries have emerged as promising alternatives.[1-5] In nature, the cornerstone reactions in these technologies are the oxygen evolution reactions (OER) and reduction reaction (ORR).[6-8] However, the sluggish reaction kinetics and the multiple proton-couple electron transfer steps in OER/ORR have severely hampered the widespread and large-scale applications of these renewable energy technologies.[9, 10] Noble metals such as ruthenium/iridium-based nanocomposites represent the most efficient commercial electrocatalysts for OER, but have limited activity for ORR. In the case of platinum and iridium alloys or oxides these materials are typically the most efficient ORR catalysts, however the poor stability and scarcity of these noble metal-based electrocatalyst remain challenges.[11, 12] It is difficult to achieve both acceptable OER and ORR activities with the same material. Therefore, the development of low-cost, efficient and durable bi-functional materials for oxygen electrocatalysis is particularly important.

Transition metals composited with N-doped carbons (M/N-C) represent a promising a material platform alternative to noble metal electrocatalysts for OER/ORR which have received wide attention.[13-15] The catalytic performance of M/N-Cs are dependent on the dispersion of metal catalytic particles and the nature of N-doped carbons. Therefore, it is important to prepare M/N-C with fine dispersions of metal nanoparticles with high electron conductivity and N-Cs surface area. Metal-organic frameworks (MOFs), featured with large surface areas, tunable pore structures and abundant N species have been investigated as precursors for producing M/N-C.[16-19] To date, various types of M/N-Cs such as Co-MOF-derived Co@N-doped C,[20] a hybrid

Fe_3C@NCNT/NPC[21] have been developed and tested as oxygen electrocatalysts. To further increase the catalytic activity, bimetallic zeolitic imidazolate frameworks (BMZIF) were introduced as templates to prepare bimetallic N-doped carbons (BM/N-C).[22-24] Many works have just focused on structural design, such as hybrid, composite or core-shell structures [25, 26]. For example, Zheng et al.[27] used a method based on thermal conversion of zeolitic imidazolate frameworks (ZIF-67) pre-grown on $Cu(OH)_2$ nanowires to prepare CuCo-embedded nitrogen-enriched mesoporous carbon framework (CuCo@NC), exhibiting improved electrocatalytic performance. However, the catalytic activity of Cu is not good compared with other transition metals, which often requires the introduction of more active transition metals[28, 29] for improving the catalytic performance. In addition, the mechanism of introducing a second metal based on Co-MOF has not been well investigated.

On the other hand, in N doped carbonaceous materials, the N tends to be in three types of dopants: quaternary, pyrrolic and pyridinic.[30-34] Since the pyridinic N has a lone pair of electrons, they can be donated to the conjugated π bond in the planar structure of carbon[35-37], leading to considerably increased catalytic activities compared to other forms of N as a dopant. This means that by increasing the levels of pyridinic N doping in carbon, the catalytic activity of N-doped carbonaceous catalysts can be improved.[6, 38, 39] In general, N doping is carried out by high temperature treatment of mixed nitrogen source but N does not appear to fully diffuse into each molecular target, resulting in poor doping levels. Alternatively, MOFs do contain a good amount of nitrogen sources within their molecular skeleton, which is beneficial to achieve high N doping. However, the amount of N in the MOF is still finite, so it is particularly important to increase the proportion of pyridinic form of N in the resultant MOF derived N-C.

In light of what discussed above, we here report the synthesis of bimetallic nanocrystals enclosed into N-doped carbon nanotubes (Ni_xCo_3@N-CN) as electrocatalyst by introducing Ni into Co-based MOF as precursors. The synthetic method of the Ni_xCo_3@N-CN is illustrated in **Figure 1**. The structure and composition of the Ni_xCo_3@N-CN were regulated by varying the molar ratio of Ni/Co. First, the precursor Ni_xCo_3-MOF was prepared by adding Co and Ni ions simultaneously. Then, the obtained Ni_xCo_3-MOF was calcined to generate Ni_xCo_3@N-CN. The morphology and composition before and after calcination were investigated systematically for catalyst morphology and structure. The results showed that the presence of Ni in the bimetallic nanocrystals is conducive

to increase the amount of pyridinic nitrogen. With an optimal Ni/Co mole ratio of 1/3, the resultant Ni_1Co_3@N-CN exhibited the highest the amount of pyridinic nitrogen of 5.62 % and ultrafine bimetallic nanocrystals with a size of ~8 nm. When tested as catalyst for OER/ORR, the Ni_1Co_3@N-CN delivered excellent catalytic activity and durability, which were comparable to the standard 20% Pt/C and RuO_2. This is attributed to a synergistic effect of bimetallic nanoparticles and N-CN network that improve the exposure of more catalytic active sites and to promote electron conduction and ion diffusion. Therefore, the prepared Ni_1Co_3@N-CN catalysts represent a low-cost and high performance material platform for renewable energy devices. This work also provides new insights into the mechanism of bimetallic MOF derived N-doping carbon for bifunctional oxygen catalysts.

Experimental Section

Synthesis of Ni_xCo_3@N-CN catalysts: All reagents were analytical grade and used without any further purification. In a typical synthesis, 12 mmol of 2-methylimidazole (MeIM) was dissolved in 100 mL of methanol to form a uniform solution, which was slowly poured into a 80 mL methanol solution containing $Co(NO_3)_2 \cdot 6H_2O$ and $Ni(NO_3)_2 \cdot 6H_2O$. The mixture was then magnetically stirred for 12 h at room temperature and purple precipitates of Ni_xCo_3-MOF precursors were then obtained by centrifuging and washing with methanol several times, where x (x=0, 0.5, 1, 2, 3) represents the amount of Ni ions in the reactants. Finally, the samples were dried in a vacuum at 60 ℃ for 24 h, followed by annealing at 900 ℃ (ramp rate of 5 ℃/min) for 2h under a N_2 atmosphere to obtain the materials in a powder form.

Sample characterization: The morphology and microstructure of the samples were assessed by scanning electron microscopy (SEM, Hitachi S4800). Transmission electron microscopy (TEM, JEM-200CX) and high-resolution transmission electron microscopy (HRTEM, JEOL-2100F) images were obtained using an accelerating voltage of 200 kV. The X-ray diffraction (XRD, Burker D8 Advance) patterns were recorded to analyze the crystal structure. X-ray photoelectron spectroscopy (XPS, ESCALAB 250) was performed by X-ray scanning, using an Al Kα line as the standard. Raman spectroscopy (Renishaw UK) was performed using a 514 nm excitation wavelength. The Brunauer-Emmett-Teller (BET) specific surface area measurements were performed by using the N_2 adsorption-desorption isotherm in a relative pressure on a NOVA 2000e. The electrochemical data and properties of the sample were measured using CHI 760E

electrochemical workstation (CHI Instruments).

Electrochemical measurement: All electrochemical analyses were measured in a three-electrode system. Ag/AgCl electrode and Platinum foil were used as the reference and counter electrodes. A glassy carbon electrode (d=4 mm) was used as the working electrode which was loaded with different samples (active materials). To prepare the working electrode, 5 mg of the active material was dispersed in a solution containing 800 μL of ethanol, 200 μL of deionized water and 10 μL of Nafion (5 wt%), ultrasonically dispersed for 30 min. Then the homogeneous catalyst ink (15 μL) was dropped onto the cleaned glassy carbon electrode surface with a mass loading of 0.58 mg/cm^2. Another set of electrodes using commercially available 20 wt% Pt/C and RuO_2 with a loading of 0.2 mg/cm^2 was also measured for comparison, with all the electrochemical data compared to the reversible hydrogen electrode (RHE) with following equation[40]:

$$E_{(RHE)} = E_{(SCE)} + E_{(Ag/AgCl)} + 0.059\ pH$$

For the ORR performance test, N_2 or O_2 was used in the electrolyte of 0.1M KOH to achieve a N_2 and O_2 saturated solution. The cyclic voltammetry (CV) curves were obtained in the N_2 and O_2 saturated solution with a scan rate of 10 mV/s. Linear sweep voltammogram (LSV) curves were measured by using a rotating disk electrode (RDE) with different rotating speeds from 400 to 2400 RPM. To further analyze and verify the electrocatalytic performance of the active materials, the electron transfer number (n) was calculated according to the Koutecky-Levich equation[41]:

$$1/J = 1/J_0 + 1/J_K = 1/(B\omega^{1/2}) + 1/J_K$$

$$B = 0.62nFAD_0^{2/3}V^{-1/6}C_0$$

Where J, J_0 and J_K represent measured current density, kinetic and diffusion-limiting current, respectively. ω is the electrode rotation rate (rad s^{-1}). F represents the Faraday constant (96,485 C mol^{-1}). A is the electrode surface (0.07065 cm^2). D_0 is the diffusion coefficient of O_2 saturated in 0.1 M KOH solution (1.9×10^{-5} cm^2 s^{-1}). V represents the kinematic viscosity constant of the electrolyte (0.01 cm^2 s^{-1}). C_0 is the O_2 saturated concentration in electrolyte (1.2×10^{-6} mol cm^{-3}).

Results and discussions

A series of Ni_xCo_3@N-CN samples were prepared via carbonizing the precursors of Ni_xCo_3-MOF with different molar ratios of Ni/Co as schematically depicted in **Figure 1**. SEM images (**Figure 2a** and **Figure S1a, c, e, g, i)** confirm that Ni_xCo_3-MOF particles have a prismatic

dodecahedron morphology with high uniformity, smooth surface and a size range ~300-500 nm. The samples containing no or less Ni (x=0, 0.5) showed an increased tendency of aggregation as the particles appear to be densely clustered and fused (**Figure S1b and d**). When the ratio of Ni/Co was 1/3, the obtained samples displayed Ni_xCo_3-MOF particles without much aggregation, which shows that moderate amounts of Ni tended to improve the quality of bimetallic particles in terms of their morphology. After pyrolysis at 900 °C, the samples Ni_1Co_3@N-CN still reflect the overall morphology of Ni_xCo_3-MOF particles but contain much smaller Ni_1Co_3 bimetallic nanoparticles, and are covered with carbon nanotubes that encase those smaller Ni_1Co_3 particles. The Ni_1Co_3@N-CN sample with a 1/3 Ni/Co ratio showed even dispersion and was wrapped with dense and netted carbon nanotubes (**Figure 2b**). With the increase of Ni content (x=2, 3), large amounts of metal clusters were observed on the surface of the particles (**Figure S1h and j**). It may be that the effect of high concentration of Ni metal ion lead to the partial segregation[42]. Therefore, it appears that a ratio of Ni/Co=1/3 is optimal for the final morphology and crystalline structure of the samples obtained in these experiments. This is further reflected in the elemental mapping (**Figure S2**) that Ni_1Co_3@N-CN particles were mainly made up of Co, Ni, C and N, and with all these elements are dispersed homogeneously.

The microstructure of the Ni_1Co_3@N-CN was analyzed by TEM. From the low-revolution TEM (**Figure S3a**), it can be observed that Ni_1Co_3@N-CN particles tended to maintain the original skeleton of the Ni_xCo_3-MOF. This is despite the original dodecahedron morphology being distorted as the particles were reduced in size and enveloped by carbon nanotubes. TEM images also showed that many carbon nanotubes were grown on the surface of the Ni_1Co_3@N-CN (**Figure S3b**). In the HRTEM analysis (**Figure 2c**), it is observable that the diameter of carbon nanotubes was ~10 nm, the length was ~60 nm and many domains of bimetallic nanoparticles with a size ~8nm were wrapped in carbon nanotubes. **Figure 2d** and **e** showed the lattice fringes with interplanar distances of 0.35 nm, 0.205 nm and 0.203 nm, which can be attributed to the C (002), Co (111) and Ni (111) planes. This is in agreement with the XRD pattern, showing the presence of bimetallic nanoparticles in carbon nanotubes. As shown in **Figure 2f**, the peaks located at about 44.2°, 51.5° and 75.8° coming from the (111), (200) and (220) planes of metal Co (JCPDS Card no. 89-7093), respectively. Similarly, the peaks at around 44.3°, 51.6° and 76.1° are attributed to the (111), (200) and (220) planes of metal Ni (JCPDS Card no. 89-7128), respectively. In addition, the XRD patterns revealed

some weak diffraction peaks at around 26.4° indexed to the typical (002) planes of graphitic carbon (JCPDS Card no. 41-1487, **Figure S4**).

Raman spectra for the Ni_xCo_3@N-CN were obtained as shown in **Figure 3a**. All the samples displayed two clear main peaks around 1,342 and 1,589 cm^{-1}, which suggests the presence of disordered carbon (from the D peak) and graphitic carbon (from the G peak)[43, 44], respectively. The intensity ratio of I_D/I_G can be used to evaluate the degree of structural disorder and defects in the carbon formed in these samples. Compared with the $Ni_{0.5}Co_3$@N-CN (I_D/I_G =1.02) and Ni_2Co_3@N-CN (I_D/I_G =1.01), the Ni_1Co_3@N-CN exhibits the highest I_D/I_G values up to 1.06, which is indicative of Ni_1Co_3@N-CN having the highest concentration of defect sites. These defects in turn can afford more active sites for an efficient electrocatalytic process. The small peaks located at ~486 and 510 cm^{-1} were attributed to the Co and Ni bonding.

The porosity of the Ni_xCo_3@N-CN structures were analyzed via N_2 adsorption-desorption isotherms as shown in **Figure 3b**. Here, the obtained isotherms displayed a distinct hysteresis loop that corresponds to the type-IV isotherm characteristics, implying the presence of mesoporous carbon structures in the Ni_xCo_3@N-CN samples. The calculated BET surface area follows the order: Ni_1Co_3@N-CN (461.9 m^2/g) > $Ni_{0.5}Co_3$@N-CN (425.7 m^2/g) > Ni_2Co_3@N-CN (389.1 m^2/g). Moreover, the pore size distribution curves (**Figure S5**) show that the Ni_1Co_3@N-CN exhibited a relatively narrow mesopore distribution while $Ni_{0.5}Co_3$@N-CN and Ni_2Co_3@N-CN possessed a broad pore size distribution. These results can in part be explained by the optimal amount of Ni being added which was beneficial to produce uniform nanoparticles and carbon nanotubes leading to the increase of the surface area and defect concentration. Such microstructures can in fact favor the contact between catalytic sites and reactants leading to improved mass transport.

The surface chemical composition of these samples was characterized by XPS. **Figure 3c** shows the full energy spectra of the Ni_xCo_3@N-CN, demonstrating the presence of Co, Ni, N and C elements. The high-resolution spectrum of Co for Ni_xCo_3@N-CN involved two main peaks (Co^0 and Co^{2+}) and two satellite peaks (**Figure 3d**). The detected Co^{2+} was attributed to the oxidization of Co when exposed to the air. Fitting of the N 1s spectra (**Figure 3e**) revealed that the N doping mainly occurred in three types: pyridinic N (398.5 eV), pyrrolic N (399.6 eV) and graphitic N (402.5 eV). Notably, Ni_1Co_3@N-CN contained the highest amount of pyridinic N (5.62 atomic% in overall elements). This result indicates that the moderate Ni addition (1/3 ratio) was conducive to fixate the

nitrogen and form pyridinic N, which can greatly improve the electronic conductivity of the Ni_1Co_3@N-CN and is expected to further enhance the catalytic activity of Ni_1Co_3@N-CN.

With the promising structural features of the samples discussed above, the performance of Ni_xCo_3@N-CN as electrocatalysts toward OER/ORR was systematically tested and analyzed. The OER activity was first recorded by LSV curves with a traditional three-electrode cell in a 1.0 M KOH solution at a scan rate of 5 mV/s (**Figure 4a**). The LSV curves showed that Ni_1Co_3@N-CN catalysts were able to achieve the lowest OER onset potential of 1.52 V (V vs RHE) compared to that of Ni_0Co_3@N-CN (1.90 V), $Ni_1Co_{0.5}$@N-CN (1.63 V), Ni_2Co_3@N-CN (1.55 V) and Ni_3Co_3@N-CN (1.57 V) at current density of 10 mA/cm^2 as shown in **Figure 4b.** According to Volmer and Heyrovsky[45], the Tafel slope indicates the exchange of electrons and desorption of OH^- from active material surfaces. Therefore, the Tafel plots were fitted from the LSV curves to study the catalytic OER kinetics. **Figure 4c** depicted the Tafel slope for the Ni_1Co_3@N-CN was 56 mV/dec, which was the smallest among the Ni_xCo_3@N-CN catalysts (169 mV/dec for Ni_0Co_3@N-CN, 106 mV/dec for $Ni_{0.5}Co_3$@N-CN, 89 mV/dec for Ni_2Co_3@N-CN and 82 mV/dec for Ni_3Co_3@N-CN). This indicated that the reactions on Ni_1Co_3@N-CN were accompanied by the fastest OER kinetics. This catalytic performance was also compared with commercial RuO_2. The results showed that the optimized Ni_1Co_3@N-CN exhibited low potential and Tafel slope, which is comparable to that of RuO_2 (Table S1). This OER performance of the Ni_1Co_3@N-CN observed here has several advantages compared with other related catalytic materials (**Tables S1**). As the catalytic activity is closely related with the electrochemical active surface area (ECSA), cyclic voltammetry (CV) curves were recorded to investigate the double layer capacitance (C_{dl}) for associated with the ECSA (**Figure S6**). The calculated C_{dl} value for Ni_1Co_3@N-CN was 10.87 mF/cm^2, which was higher than that for other Ni_xCo_3@N-CN materials (**Figure 4d**). This revealed that the Ni_1Co_3@N-CN possessed a higher surface area and thus more catalytic active sites. The long-term durability was assessed through galvanostatic tests with repeated LSV curves. **Figure 4e** showed that Ni_1Co_3@N-CN can maintain a stable potential after 35,000s. Further repeating 2,000 LSV tests, the potential for Ni_1Co_3@N-CN only increased by a negligible value (**Figure 4f**), demonstrating the excellent durability of Ni_1Co_3@N-CN.

The ORR property of Ni_xCo_3@N-CN was then investigated on a RDE in alkali media. The ORR electrocatalytic activity was studied by CV curves compared under N_2 and O_2. All the

Ni_xCo_3@N-CN samples showed a well-defined cathodic peak between 0.8 and 0.9 V in an O_2-saturated solution, evidencing their ORR catalytic activity (**Figure 5a and Figure S7**). Comparing the cathodic peak current density, it can be seen that that the Ni_1Co_3@N-CN exhibited the highest current density, an indicator for higher ORR activity. The LSV curves were collected to further analyze the ORR at the rotation speed of 1,600 RPM. As shown in **Figure 5b** and **c**, the Ni_1Co_3@N-CN displayed a lower half-wave potential ($E_{1/2}$ = 0.71 V) than that of other Ni_xCo_3@N-CN (Ni_0Co_3@N-CN: 0.85 V, $Ni_{0.5}Co_3$@N-CN: 0.82 V; Ni_2Co_3@N-CN: 0.79 V and Ni_2Co_3@N-CN: 0.80 V). The limiting current density for the Ni_1Co_3@N-CN was 4.2 mA/cm^2, which greatly exceeded its counterparts and approached that of the state-of-art 20 % Pt/C. In order to explore the ORR electron-transfer mechanism, LSV curves with different rotation speeds from 400 to 2,400 RPM were collected (**Figure 5d and Figure S8**). The electron transfer numbers (*n*) were calculated based on the Koutecky-Levich (K-L) equation from LSV curves. The specific *n* varied from 3.75, 3.86, 4.06, 3.98 to 3.82 for all the Ni_xCo_3@N-CN (**Figure 5e and Figure S8**). The *n* for Ni_1Co_3@N-CN was close to that of the theoretical value of 4 for the oxygen reduction pathway for the ORR. In addition, the limiting current densities increased with rotation speed simultaneously, suggesting the diffusion controlled processes. All in all, the ORR properties of Ni_1Co_3@N-CN have many advantages compared with other related materials (**Tables S1**). The stability for ORR performance was also recorded by current-time measurement (*i-t*). As shown in **Figure 5f**, the current retention rate of Ni_1Co_3@N-CN can be as high as 86.6 % over a 25,000s test, indicating excellent ORR durability.

Finally Ni_1Co_3@N-CN was tested as catalyst for both the electrodes in a cell (for both OER and ORR). The cell based on Ni_1Co_3@N-CN catalysts showed a wider potential window than that of commercial Pt/C//RuO_2 (**Figure S9**). This outstanding result obtained with Ni_1Co_3@N-CN as a bifunctional oxygen electrocatalyst can be attributed to the optimal Ni in bimetallic, which aided high pyridinic N doping along with other microstructural features discussed above.

Conclusions

In this work, a synthesis route to obtain bifunctional oxygen electrocatalysts, namely Ni_xCo_3@N-CN, consisting of high amounts of pyridinic N-doped carbon nanotubes (N-CN) and cobalt nickel (Ni_xCo_3) bimetallic nanocrystals with a metal-organic framework was developed. The optimal amount of Ni in the Ni_1Co_3 bimetallic nanoparticles was shown to be conducive to enhancing the

doping of pyridinic nitrogen, a crucial factor for achieving high electrocatalytic activity. With an optimal Co/Ni molar ratio of 3:1, the Ni_1Co_3@N-CN composites exhibited ultrafine nanocrystals with a size of ~8 nm and pyridinic nitrogen content as high as 5.62 %. When tested as an OER electrocatalyst, Ni_1Co_3@N-CN showed a decreased OER onset potential ~1.52 V at the current density of 10 mA/cm^2 and improved kinetics (a lower Tafel slope of 56 mV/decade). In ORR tests, Ni_1Co_3@N-CN electrocatalysts enabled a favorable half-wave potential of 0.85 V and a larger limiting current density of 4.73 mA/cm^2, both of which demonstrate not only superior oxygen electrocatalytic performance compared to many similar catalysts but it is possible to achieve both ORR and OER activities by using a single bifunctional oxygen electrocatalytic system. These results can stimulate further research towards the development of low-cost and high performance bifunctional electrocatalysts via metal organic frameworks. These results also implies that as prepared Ni_xCo_3@N-CN composites can play a significant role in rechargeable metal-air batteries.

Supporting Information

SEM of Ni_xCo_3-MOF and Ni_xCo_3@N-CN; EDS mappings and TEM images of Ni_1Co_3@N-CN; XRD patterns and pore size distribution of Ni_xCo_3@N-CN with different proportions; CV and LSV curves of obtained samples; and summary of the relative materials with OER and ORR performances.

Conflicts of interest

There are no conflicts to declare.

Acknowledgments

The financial supports for this research are the Postdoctoral research projects of Jiangxi University of Science and technology (No 3205700011), High-Level talent funds (No. 3401223254) and the specialized research fund for the doctoral program (No.3401223242 and No. 3203304894). XL and BW thank the EPSRC energy storage for low carbon grids project (EP/K002252/1), the EPSRC Joint UK - India Clean Energy Centre (JUICE) (EP/P003605/1) and the IDLES project (EP/R045518/1). The Royal Society is acknowledged for an URF (of CG).

References

1. Suntivich, J.; May, K. J.; Gasteiger, H. A.; Goodenough, J. B.; Shao-Horn, Y., A Perovskite Oxide Optimized for Oxygen Evolution Catalysis from Molecular Orbital Principles. *Science* **2011,** *334* (6061), 1383-1385.
2. Bruce, P. G.; Freunberger, S. A.; Hardwick, L. J.; Tarascon, J. M., Li-O-2 and Li-S batteries with high energy storage. *Nature materials* **2012,** *11* (1), 19-29.
3. Suntivich, J.; Gasteiger, H. A.; Yabuuchi, N.; Nakanishi, H.; Goodenough, J. B.; Shao-Horn, Y., Design principles for oxygen-reduction activity on perovskite oxide catalysts for fuel cells and metal-air batteries. *Nat Chem* **2011,** *3* (7), 546-550.
4. Hou, Y.; Yuan, H. Y.; Wen, Z. H.; Cui, S. M.; Guo, X. R.; He, Z.; Chen, J. H., Nitrogen-doped graphene/CoNi alloy encased within bamboo-like carbon nanotube hybrids as cathode catalysts in microbial fuel cells. *J Power Sources* **2016,** *307*, 561-568.
5. Fu, G. T.; Chen, Y. F.; Cui, Z. M.; Li, Y. T.; Zhou, W. D.; Xing, S.; Tang, Y. W.; Goodenough, J. B., Novel Hydrogel-Derived Bifunctional Oxygen Electrocatalyst for Rechargeable Air Cathodes. *Nano letters* **2016,** *16* (10), 6516-6522.
6. Yang, H. B.; Miao, J. W.; Hung, S. F.; Chen, J. Z.; Tao, H. B.; Wang, X. Z.; Zhang, L. P.; Chen, R.; Gao, J. J.; Chen, H. M.; Dai, L. M.; Liu, B., Identification of catalytic sites for oxygen reduction and oxygen evolution in N-doped graphene materials: Development of highly efficient metal-free bifunctional electrocatalyst. *Sci Adv* **2016,** *2* (4).
7. Zhang, P.; Zhao, Y.; Zhang, X. B., Functional and stability orientation synthesis of materials and structures in aprotic Li-O-2 batteries. *Chemical Society reviews* **2018,** *47* (8), 2921-3004.
8. Zhao, Q.; Yan, Z. H.; Chen, C. C.; Chen, J., Spinels: Controlled Preparation, Oxygen Reduction/Evolution Reaction Application, and Beyond. *Chem Rev* **2017,** *117* (15), 10121-10211.
9. Suen, N. T.; Hung, S. F.; Quan, Q.; Zhang, N.; Xu, Y. J.; Chen, H. M., Electrocatalysis for the oxygen evolution reaction: recent development and future perspectives. *Chemical Society reviews* **2017,** *46* (2), 337-365.
10. Jin, H. Y.; Guo, C. X.; Liu, X.; Liu, J. L.; Vasileff, A.; Jiao, Y.; Zheng, Y.; Qiao, S. Z., Emerging Two-Dimensional Nanomaterials for Electrocatalysis. *Chem Rev* **2018,** *118* (13), 6337-6408.
11. Dai, L. M.; Xue, Y. H.; Qu, L. T.; Choi, H. J.; Baek, J. B., Metal-Free Catalysts for Oxygen Reduction Reaction. *Chem Rev* **2015,** *115* (11), 4823-4892.
12. Reier, T.; Oezaslan, M.; Strasser, P., Electrocatalytic Oxygen Evolution Reaction (OER) on Ru, Ir, and Pt Catalysts: A Comparative Study of Nanoparticles and Bulk Materials. *Acs Catal* **2012,** *2* (8), 1765-1772.
13. Zou, X. X.; Huang, X. X.; Goswami, A.; Silva, R.; Sathe, B. R.; Mikmekova, E.; Asefa, T., Cobalt-Embedded Nitrogen-Rich Carbon Nanotubes Efficiently Catalyze Hydrogen Evolution Reaction at All pH Values**. *Angew Chem Int Edit* **2014,** *53* (17), 4372-4376.
14. Ning, H. H.; Li, G. Q.; Chen, Y.; Zhang, K. K.; Gong, Z.; Nie, R. F.; Hu, W.; Xia, Q. H., Porous N-Doped Carbon-Encapsulated CoNi Alloy Nanoparticles Derived from MOFs as Efficient Bifunctional Oxygen Electrocatalysts. *ACS applied materials & interfaces* **2019,** *11* (2), 1957-1968.
15. Yasuda, S.; Furuya, A.; Uchibori, Y.; Kim, J.; Murakoshi, K., Iron-Nitrogen-Doped Vertically Aligned Carbon Nanotube Electrocatalyst for the Oxygen Reduction Reaction. *Adv Funct Mater* **2016,** *26* (5), 738-744.

16. Liu, S. H.; Wang, Z. Y.; Zhou, S.; Yu, F. J.; Yu, M. Z.; Chiang, C. Y.; Zhou, W. Z.; Zhao, J. J.; Qiu, J. S., Metal-Organic-Framework-Derived Hybrid Carbon Nanocages as a Bifunctional Electrocatalyst for Oxygen Reduction and Evolution. *Advanced Materials* **2017,** *29* (31).
17. Xia, B. Y.; Yan, Y.; Li, N.; Wu, H. B.; Lou, X. W.; Wang, X., A metal-organic framework-derived bifunctional oxygen electrocatalyst. *Nat Energy* **2016,** *1*.
18. Wang, C.; Liu, D. M.; Lin, W. B., Metal-Organic Frameworks as A Tunable Platform for Designing Functional Molecular Materials. *Journal of the American Chemical Society* **2013,** *135* (36), 13222-13234.
19. Meng, J. S.; Niu, C. J.; Xu, L. H.; Li, J. T.; Liu, X.; Wang, X. P.; Wu, Y. Z.; Xu, X. M.; Chen, W. Y.; Li, Q.; Zhu, Z. Z.; Zhao, D. Y.; Mai, L. Q., General Oriented Formation of Carbon Nanotubes from Metal-Organic Frameworks. *Journal of the American Chemical Society* **2017,** *139* (24), 8212-8221.
20. Zhu, Q. L.; Xia, W.; Akita, T.; Zou, R. Q.; Xu, Q., Metal-Organic Framework-Derived Honeycomb-Like Open Porous Nanostructures as Precious-Metal-Free Catalysts for Highly Efficient Oxygen Electroreduction. *Advanced Materials* **2016,** *28* (30), 6391-+.
21. Zhao, P. P.; Hua, X.; Xu, W.; Luo, W.; Chen, S. L.; Cheng, G. Z., Metal-organic framework-derived hybrid of Fe3C nanorod-encapsulated, N-doped CNTs on porous carbon sheets for highly efficient oxygen reduction and water oxidation. *Catal Sci Technol* **2016,** *6* (16), 6365-6371.
22. Li, Y. L.; Jia, B. M.; Fan, Y. Z.; Zhu, K. L.; Li, G. Q.; Su, C. Y., Bimetallic Zeolitic Imidazolite Framework Derived Carbon Nanotubes Embedded with Co Nanoparticles for Efficient Bifunctional Oxygen Electrocatalyst. *Adv Energy Mater* **2018,** *8* (9).
23. Chen, Y. Z.; Wang, C. M.; Wu, Z. Y.; Xiong, Y. J.; Xu, Q.; Yu, S. H.; Jiang, H. L., From Bimetallic Metal-Organic Framework to Porous Carbon: High Surface Area and Multicomponent Active Dopants for Excellent Electrocatalysis. *Advanced Materials* **2015,** *27* (34), 5010-5016.
24. Wang, T.; Jin, R. M.; Wu, X. Q.; Zheng, J.; Li, X. G.; Ostrikov, K., A highly efficient Ni-Mo bimetallic hydrogen evolution catalyst derived from a molybdate incorporated Ni-MOF. *J Mater Chem A* **2018,** *6* (19), 9228-9235.
25. Wang, Z. J.; Lu, Y. Z.; Yan, Y.; Larissa, T. Y. P.; Zhang, X.; Wuu, D.; Zhang, H.; Yang, Y. H.; Wang, X., Core-shell carbon materials derived from metal-organic frameworks as an efficient oxygen bifunctional electrocatalyst. *Nano Energy* **2016,** *30*, 368-378.
26. Pan, Y.; Sun, K. A.; Liu, S. J.; Cao, X.; Wu, K. L.; Cheong, W. C.; Chen, Z.; Wang, Y.; Li, Y.; Liu, Y. Q.; Wang, D. S.; Peng, Q.; Chen, C.; Li, Y. D., Core-Shell ZIF-8@ZIF-67-Derived CoP Nanoparticle-Embedded N-Doped Carbon Nanotube Hollow Polyhedron for Efficient Overall Water Splitting. *Journal of the American Chemical Society* **2018,** *140* (7), 2610-2618.
27. Kuang, M.; Wang, Q. H.; Han, P.; Zheng, G. F., Cu, Co-Embedded N-Enriched Mesoporous Carbon for Efficient Oxygen Reduction and Hydrogen Evolution Reactions. *Adv Energy Mater* **2017,** *7* (17).
28. Wang, J.; Liu, W.; Luo, G.; Li, Z. J.; Zhao, C.; Zhang, H. R.; Zhu, M. Z.; Xu, Q.; Wang, X. Q.; Zhao, C. M.; Qu, Y. T.; Yang, Z. K.; Yao, T.; Li, Y. F.; Lin, Y.; Wu, Y.; Li, Y. D., Synergistic effect of well-defined dual sites boosting the oxygen reduction reaction. *Energ Environ Sci* **2018,** *11* (12), 3375-3379.
29. Li, X.; Wang, X. L.; Zhou, J.; Han, L.; Sun, C. Y.; Wang, Q. Q.; Su, Z. M., Ternary hybrids as efficient bifunctional electrocatalysts derived from bimetallic metal-organic-frameworks for overall water splitting. *J Mater Chem A* **2018,** *6* (14), 5789-5796.
30. Liu, X. B.; Wu, Z. P.; Yin, Y. H., Highly nitrogen-doped graphene anchored with Co3O4 nanoparticles as supercapacitor electrode with enhanced electrochemical performance. *Synthetic Met* **2017,** *223*, 145-152.
31. Guo, D. H.; Shibuya, R.; Akiba, C.; Saji, S.; Kondo, T.; Nakamura, J., Active sites of nitrogen-

doped carbon materials for oxygen reduction reaction clarified using model catalysts. *Science* **2016,** *351* (6271), 361-365.

32. Rao, C. V.; Cabrera, C. R.; Ishikawa, Y., In Search of the Active Site in Nitrogen-Doped Carbon Nanotube Electrodes for the Oxygen Reduction Reaction. *Journal of Physical Chemistry Letters* **2010,** *1* (18), 2622-2627.

33. Liu, X.; Dai, L. M., Carbon-based metal-free catalysts. *Nat Rev Mater* **2016,** *1* (11).

34. Li, R.; Wei, Z. D.; Gou, X. L., Nitrogen and Phosphorus Dual-Doped Graphene/Carbon Nanosheets as Bifunctional Electrocatalysts for Oxygen Reduction and Evolution. *Acs Catal* **2015,** *5* (7), 4133-4142.

35. Luo, Z. Q.; Lim, S. H.; Tian, Z. Q.; Shang, J. Z.; Lai, L. F.; MacDonald, B.; Fu, C.; Shen, Z. X.; Yu, T.; Lin, J. Y., Pyridinic N doped graphene: synthesis, electronic structure, and electrocatalytic property. *J Mater Chem* **2011,** *21* (22), 8038-8044.

36. Li, M. T.; Zhang, L. P.; Xu, Q.; Niu, J. B.; Xia, Z. H., N-doped graphene as catalysts for oxygen reduction and oxygen evolution reactions: Theoretical considerations. *J Catal* **2014,** *314*, 66-72.

37. Wang, Q. C.; Lei, Y. P.; Zhu, Y. G.; Wang, H.; Feng, J. Z.; Ma, G. Y.; Wang, Y. D.; Li, Y. J.; Nan, B.; Feng, Q. G.; Lu, Z. G.; Yu, H., Edge Defect Engineering of Nitrogen-Doped Carbon for Oxygen Electrocatalysts in Zn-Air Batteries. *ACS applied materials & interfaces* **2018,** *10* (35), 29448-29456.

38. Mamtani, K.; Jain, D.; Dogu, D.; Gustin, V.; Gunduz, S.; Co, A. C.; Ozkan, U. S., Insights into oxygen reduction reaction (ORR) and oxygen evolution reaction (OER) active sites for nitrogen-doped carbon nanostructures (CNx) in acidic media. *Appl Catal B-Environ* **2018,** *220*, 88-97.

39. Sun, J. G.; Wang, L.; Song, R. R.; Yanga, S. B., Enhancing pyridinic nitrogen level in graphene to promote electrocatalytic activity for oxygen reduction reaction. *Nanotechnology* **2016,** *27* (5).

40. Wu, H. B.; Xia, B. Y.; Yu, L.; Yu, X. Y.; Lou, X. W., Porous molybdenum carbide nano-octahedrons synthesized via confined carburization in metal-organic frameworks for efficient hydrogen production. *Nat Commun* **2015,** *6*, 6512.

41. Xia, B. Y.; Yan, Y.; Li, N.; Wu, H. B.; Lou, X. W.; Wang, X., A metal–organic framework-derived bifunctional oxygen electrocatalyst. *Nature Energy* **2016,** *1* (1), 15006.

42. Li, X.; Wang, X.; Zhou, J.; Han, L.; Sun, C.; Wang, Q.; Su, Z., Ternary hybrids as efficient bifunctional electrocatalysts derived from bimetallic metal–organic-frameworks for overall water splitting. *Journal of Materials Chemistry A* **2018,** *6* (14), 5789-5796.

43. Liu, X.; Zou, S.; Liu, K.; Lv, C.; Wu, Z.; Yin, Y.; Liang, T.; Xie, Z., Highly compressible three-dimensional graphene hydrogel for foldable all-solid-state supercapacitor. *Journal of Power Sources* **2018,** *384*, 214-222.

44. Chen, Z.; Wu, R.; Liu, Y.; Ha, Y.; Guo, Y.; Sun, D.; Liu, M.; Fang, F., Ultrafine Co Nanoparticles Encapsulated in Carbon-Nanotubes-Grafted Graphene Sheets as Advanced Electrocatalysts for the Hydrogen Evolution Reaction. *Adv Mater* **2018**, e1802011.

45. Wang, T.; Zhou, Q.; Wang, X.; Zheng, J.; Li, X., MOF-derived surface modified Ni nanoparticles as an efficient catalyst for the hydrogen evolution reaction. *Journal of Materials Chemistry A* **2015,** *3* (32), 16435-16439.

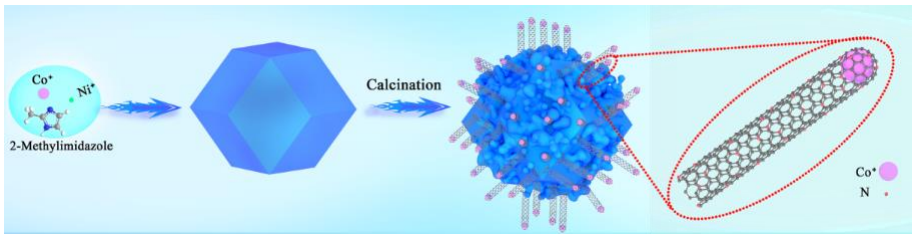

Figure 1 Schematic illustration of the synthetic route to the bimetallic nanoparticles embedded in N-doping carbon nanotubes derived from Ni-doped Co based metal-organic frameworks

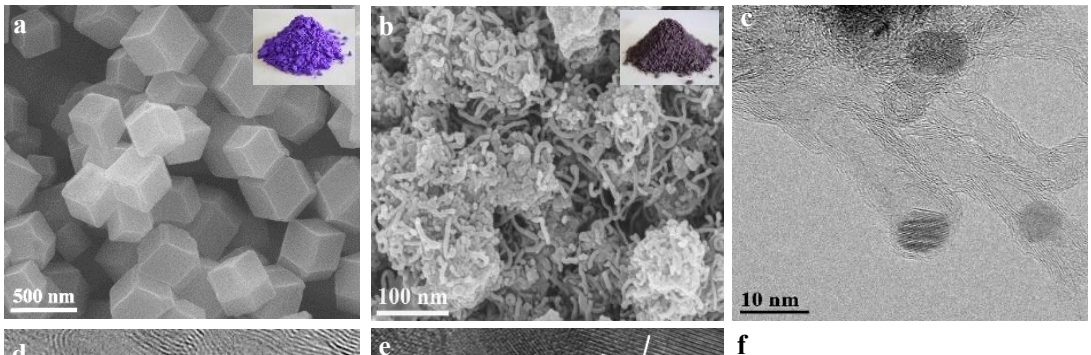

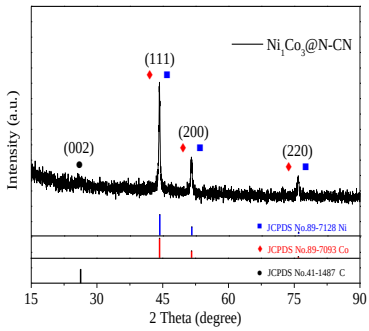

Figure 2 Scanning electron microscopic (SEM) images of (a) Ni_1Co_3-MOF precursor and (b) Ni_1Co_3@N-CN prepared from carbonizing the precursor at 900°C; (c, d) Transmission electron microscopic (TEM) and (e) high resolution TEM images (f) X ray diffraction (XRD) pattern for Ni_1Co_3@N-CN

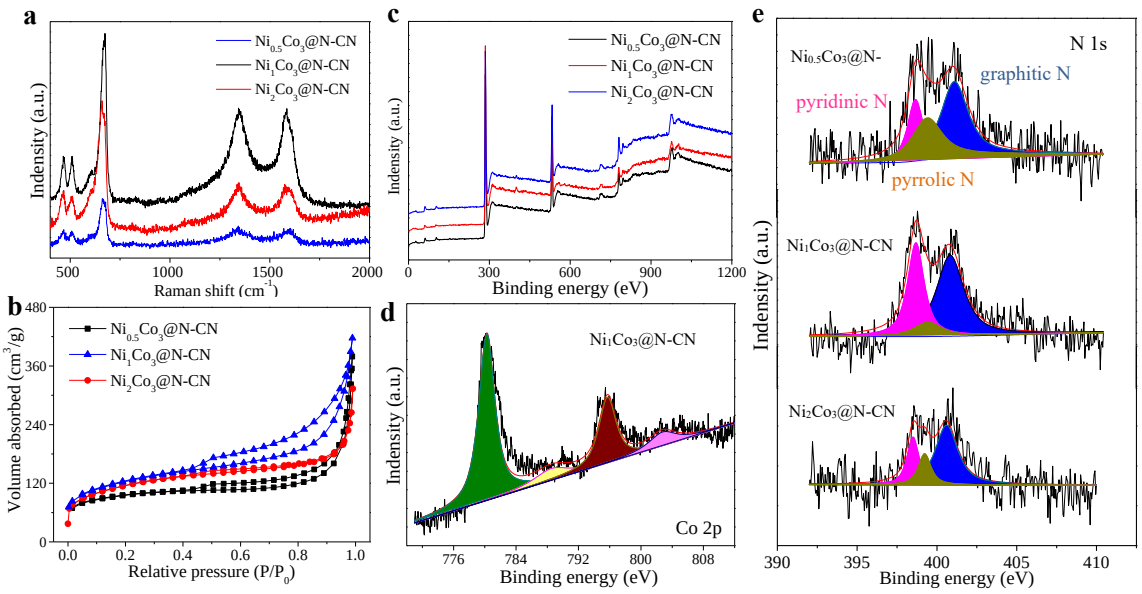

Figure 3 (a) Raman spectra, (b) N_2 adsorption-desorption isotherms and (c) X ray photoelectron spectroscopic (XPS) survey spectra for Ni_xCo_3@N-CN obtained from different Ni/Co ratios, high resolution spectra of (d) Co 2p for Ni_1Co_3@N-CN and (e) N 1s for Ni_xCo_3@N-CN, respectively

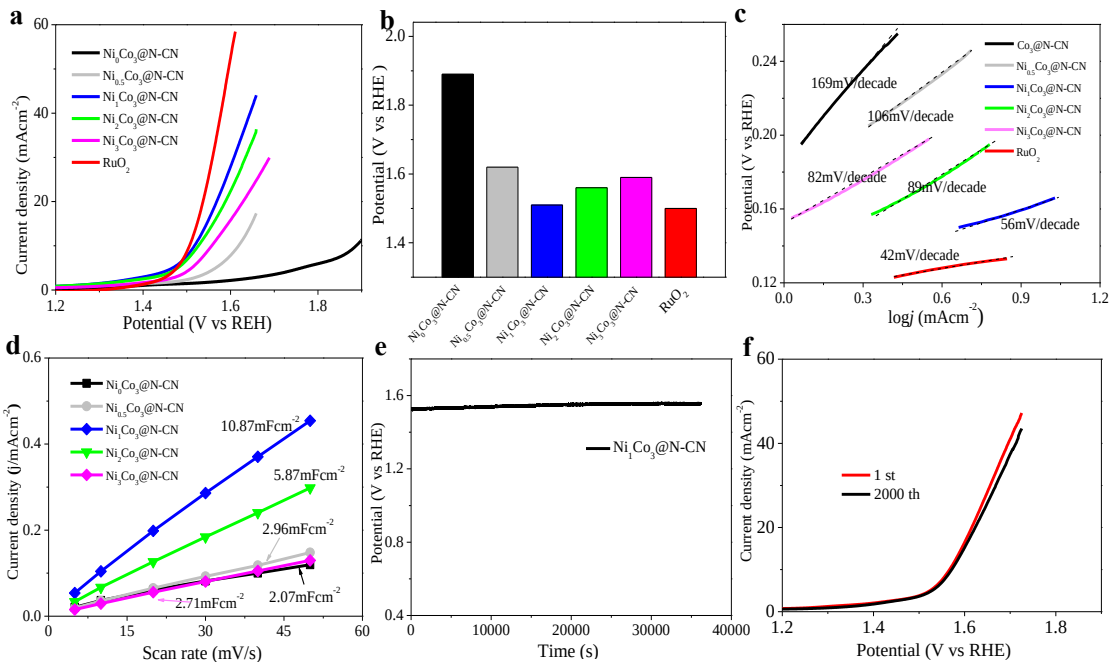

Figure 4 (a) Linear sweep voltammetry (LSV) curves, (b) comparison of the overpotential obtained a current density of 10 mA/cm^2 and (c) the corresponding Tafel plots of Ni_xCo_3@N-CN and RuO_2 catalyst (commercial) at 1M KOH solution. Scan rate 10 mV/s; (d) The capacitive current as a function of different scan rates for the various sample; (e) Long-term oxygen evolution reaction (OER) durability test of Ni_1Co_3@N-CN; and (f) LSV curves comparison of 1st and 2000th cycling

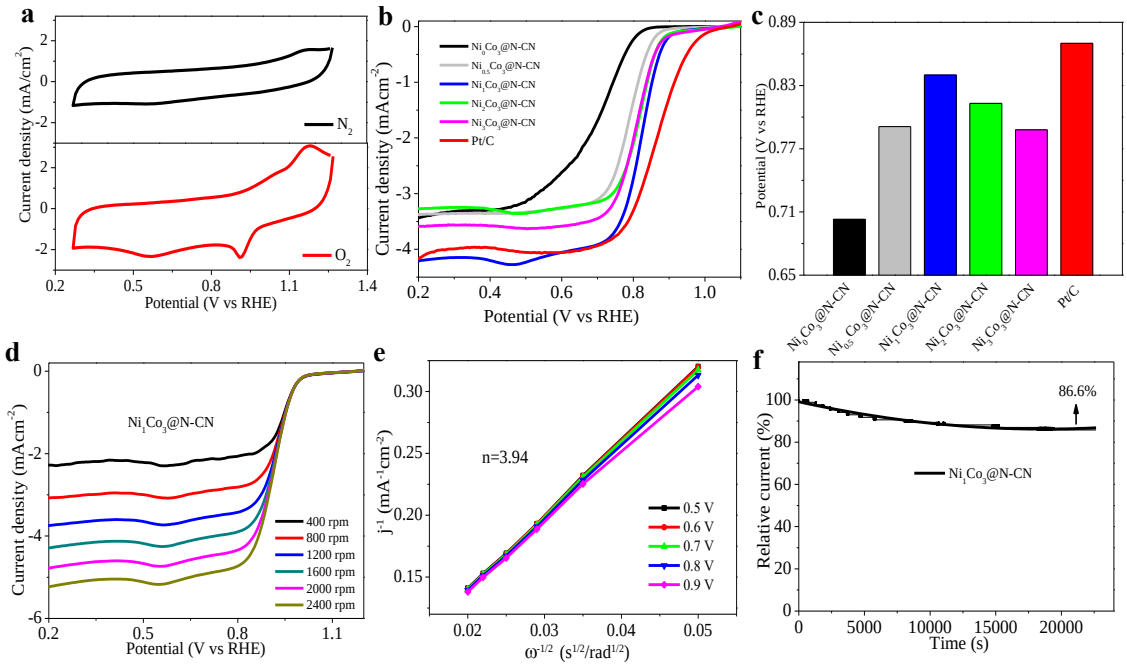

Figure 5 (a) Cyclic voltammetry (CV) curves comparison in N_2 and O_2 saturated 0.1M KOH solution and (b) Linear sweep voltammetry (LSV) curves at different rotation rates for Ni_1Co_3@N-CN; (c) Comparison of half-wave potential ($E_{1/2}$) for different catalysts; (d) LSV curves for Ni_xCo_3@N-CN and commercial Pt/C catalyst at an RDE of 1600 r.p.m (Scan rate 10 mV/s); (e) The Koutecky-levich plots at different potentials; (f) Long-term ORR durability test of the Ni_1Co_3@N-CN for 20000s